PHYSICAL REVIEW D **86,** 094014 (2012)

Constraints on flavor-changing neutral-current Htq couplings from the signal of tH associated production with QCD next-to-leading order accuracy at the LHC

Yan Wang,[1] Fa Peng Huang,[1] Chong Sheng Li,[1,2,*] Bo Hua Li,[1] Ding Yu Shao,[1] and Jian Wang[1]
[1]*Department of Physics and State Key Laboratory of Nuclear Physics and Technology,*
Peking University, Beijing 100871, China
[2]*Center for High Energy Physics, Peking University, Beijing 100871, China*
(Received 16 August 2012; published 6 November 2012)

We study a generic Higgs boson and a top quark associated production via model-independent flavor-changing neutral-current couplings at the LHC, including complete QCD next-to-leading order (NLO) corrections to the production and decay of the top quark and the Higgs boson. We find that QCD NLO corrections can increase the total production cross sections by about 48.9% and 57.9% for the Htu and Htc coupling induced processes at the LHC, respectively. After kinematic cuts are imposed on the decay products of the top quark and the Higgs boson, the QCD NLO corrections are reduced to 11% for the Htu coupling induced process and almost vanish for the Htc coupling induced process. Moreover, QCD NLO corrections reduce the dependence of the total cross sections on the renormalization and factorization scales. We also discuss signals of the tH associated production with the decay mode $t \to bl^+ \not{E}_T$, $H \to b\bar{b}$, and $t\bar{t}$ production with the decay mode $\bar{t} \to H\bar{q}$, $t \to bl^+ \not{E}_T$. Our results show that, in some parameter regions, the LHC may observe the above signals at the 5σ level. Otherwise, the upper limits on the flavor-changing neutral-current Htq couplings can be set.

DOI: 10.1103/PhysRevD.86.094014 PACS numbers: 14.65.Ha, 12.38.Bx, 12.60.Fr

I. INTRODUCTION

Recently, the ATLAS and CMS Collaborations at the Large Hadron Collider (LHC) have discovered a new particle with a mass of about 125 GeV [1,2]. In the near future, the most important task is to study the intrinsic properties of this new particle, such as the couplings and spin, which will determine whether it is the standard model (SM) Higgs boson, and lead to deeper understanding of electroweak (EW) symmetry breaking mechanism.

It is attractive to investigate the anomalous couplings of a generic Higgs boson, such as the anomalous couplings with quarks via flavor-changing neutral-current (FCNC) couplings. In the SM, FCNC couplings are absent at tree level, and is suppressed at the one-loop level by the Glashow-Iliopoulos-Maiani mechanism [3]. The anomalous couplings, if they exist, are strong evidence of new physics (NP). In Ref. [4], indirect constraints on FCNC couplings from low-energy experiments are studied and used to analyze the process of the Higgs boson decaying to light quarks or leptons. But the FCNC couplings between the Higgs boson and the top quark are not discussed there.

The top quark mass is close to the EW symmetry breaking scale. Thus, it is an appropriate probe for the EW symmetry breaking mechanism and NP. Any deviation from SM prediction for precise observables involving top quarks exhibits hints of NP. The production of a single top quark associated with a gluon jet or a vector boson via FCNC couplings has already been investigated at the leading order (LO) [5–8] and at the next-to-leading order (NLO) [9–13], respectively. In this paper, we will discuss the constraints on the FCNC Htq couplings from the signal of the Higgs boson and the top quark associated production with QCD NLO accuracy at the LHC.

In some NP models, the FCNC couplings of the Higgs boson and the top quark can be generated at tree level, or enhanced to observable levels through radiative corrections [5–14], such as the two Higgs doublet models III [15,16], the minimal supersymmetric models[17–22], the top color-assisted technicolor model [16], the exotic quarks models and the left-right symmetric models [23,24]. Since we do not know which type of NP will be responsible for the future deviation, it is better to study the FCNC processes with a model-independent method. In general, the interactions between the Higgs boson, the top quark, and a light quark q ($= u, c$) can be expressed as [5]

$$\mathcal{L} = -\frac{g}{2\sqrt{2}} \sum_{q=u,c} g_{qt}\bar{q}(g^v_{qt} + g^a_{qt}\gamma_5)tH + \text{H.c.}, \qquad (1)$$

where g_{qt} ($q = u, c$) defining the strength of the coupling is a real coefficient, while g^v_{qt}, g^a_{qt} are complex numbers, normalized to $|g^v_{qt}|^2 + |g^a_{qt}|^2 = 1$. The constraints on the above couplings have been set through indirect low-energy processes in Refs. [25–27]. It is interesting to study how to set the direct constraints on the above couplings from the signals of the top quark and the Higgs boson associated production and top pair production with top quark rare decay at the hadron colliders. These processes have been studied at the LO in Ref. [5]. However, the LO total cross sections at the hadron collider suffer from large uncertainties due to the arbitrary choices of the renormalization and

---

[*] csli@pku.edu.cn

© 2012 American Physical Society

factorization scales. Besides, at the NLO level the additional radiation makes b jets, which are the products of the Higgs boson and the top quark softer and the mass distribution of the reconstructed particles broader, which will affect events selection when kinematic cuts are imposed. Thus, it is necessary to perform complete QCD NLO calculations of these processes at the LHC, including production and decay.

The process $gb \to tH^-$, which has the similar scattering amplitude to the process we study in this paper, has been discussed in the two Higgs doublet models and supersymmetry, including the QCD NLO or supersymmetry QCD corrections [28–31]. After considering the difference from the couplings and parton distribution functions (PDFs), our numerical results for the tH production are consistent with the their results in the range of Monte Carlo integration error. However, in the process we study, the Higgs boson is neutral and has a mass around 125 GeV, usually much less than the mass of the charged Higgs boson, which leads to significantly different decay modes and signals at the hadron colliders.

The arrangement of this paper is as follows. In Sec. II, we present the LO results for the Higgs boson and the top quark associated production induced by FCNC Htq couplings. In Sec. III, we describe the detailed calculations of the NLO results, including the virtual and real corrections. Then in Sec. IV, we investigate numerical results, in which we discuss the scale uncertainties and give some important kinematic distributions. In Sec. V, we discuss the signals of tH associated production with the decay mode $t \to bl^+\nu_e$ and $H \to b\bar{b}$, and $t\bar{t}$ production with rare decay mode $\bar{t} \to Hq \to b\bar{b}q$. Then we analysis the discovery potential with QCD NLO accuracy at the LHC with $\sqrt{S} = 14$ TeV. Section VI is a brief conclusion.

II. LEADING ORDER RESULTS

At the hadron colliders, there is only one subprocess that contributes to the tH associated production at the LO via FCNC Htq couplings,

$$gq \to tH, \tag{2}$$

where q is either a u or c quark. The Feynman diagrams are shown in Fig. 1.

After summing (averaging) over the spins and colors of the final-(initial-)state particles, the explicit expression of the squared amplitude at the LO is

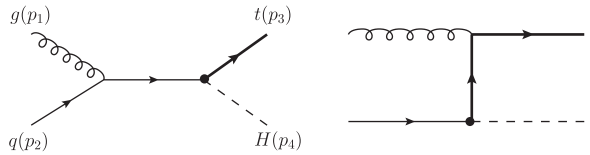

FIG. 1. The LO Feynman diagrams for tH associated production via FCNC Htq couplings.

$$\begin{aligned}\overline{|\mathcal{M}^B|^2}_{qg}(s,t) = {} & \frac{\pi^2\alpha\alpha_s g_{qt}^2}{3\sin\theta_W^2 s(t-m_t^2)^2}(m_t^6-(2m_H^2+2s+t)m_t^4 \\ & +(2m_H^4+(s+t)^2)m_t^2-2tm_H^4 \\ & +2t(s+t)m_H^2-t(s+t)^2),\end{aligned} \tag{3}$$

where m_t and m_H are the top quark mass and the Higgs boson mass, respectively. The Mandelstam variables s, t, and u are defined as

$$s=(p_1+p_2)^2, \quad t=(p_1-p_3)^2, \quad u=(p_1-p_4)^2. \tag{4}$$

The LO total cross section at hadron colliders is given by convoluting the partonic cross section with the PDFs $G_{i/P}$ in the proton,

$$\begin{aligned}\sigma^B = {} & \int dx_1 dx_2 [G_{g/P_1}(x_1,\mu_f)G_{q/P_2}(x_2,\mu_f) \\ & +(x_1 \leftrightarrow x_2)]\hat{\sigma}^B_{qg},\end{aligned} \tag{5}$$

where μ_f is the factorization scale, and $\hat{\sigma}^B_{qg} = (1/2s) \times \int \overline{|\mathcal{M}^B|^2}_{qg} dPS^{(2)}$ is Born level partonic cross section.

III. THE NEXT-TO-LEADING ORDER CALCULATIONS

In this section, we present QCD NLO corrections of tH associated production using dimensional regularization scheme with naive γ_5 prescription in $n = 4 - 2\epsilon$ dimensions to regularize the ultraviolet (UV) and infrared (IR) divergences. The NLO corrections contain the virtual gluon effects and the real radiation of a gluon or a massless quark. The corresponding Feynman diagrams are shown in Figs. 2 and 3, respectively. We use two cutoff phase space slicing method [32] in the real corrections to separate the IR divergences.

A. Virtual corrections

The virtual corrections come from the interference of the one-loop amplitude with the Born amplitude,

$$\hat{\sigma}^V = \frac{1}{2s}\int dPS^{(2)} 2\,\mathrm{Re}\,(\overline{\mathcal{M}^V \cdot \mathcal{M}^{B*}}). \tag{6}$$

We introduce counterterms to absorb UV divergences. For the external fields, we fix all of the renormalization constants using the on shell renormalization scheme,

$$\begin{aligned}\delta Z_2^{(g)} &= -\frac{\alpha_s}{2\pi}C_\epsilon\left(\frac{n_f}{3}-\frac{5}{2}\right)\left(\frac{1}{\epsilon_{\mathrm{UV}}}-\frac{1}{\epsilon_{\mathrm{IR}}}\right)-\frac{\alpha_s}{6\pi}C_\epsilon\frac{1}{\epsilon_{\mathrm{UV}}}, \\ \delta Z_2^{(q)} &= -\frac{\alpha_s}{3\pi}C_\epsilon\left(\frac{1}{\epsilon_{\mathrm{UV}}}-\frac{1}{\epsilon_{\mathrm{IR}}}\right), \\ \delta Z_2^{(t)} &= -\frac{\alpha_s}{3\pi}C_\epsilon\left(\frac{1}{\epsilon_{\mathrm{UV}}}+\frac{2}{\epsilon_{\mathrm{IR}}}+4\right), \\ \frac{\delta m_t}{m_t} &= -\frac{\alpha_s}{3\pi}C_\epsilon\left(\frac{3}{\epsilon_{\mathrm{UV}}}+4\right),\end{aligned} \tag{7}$$

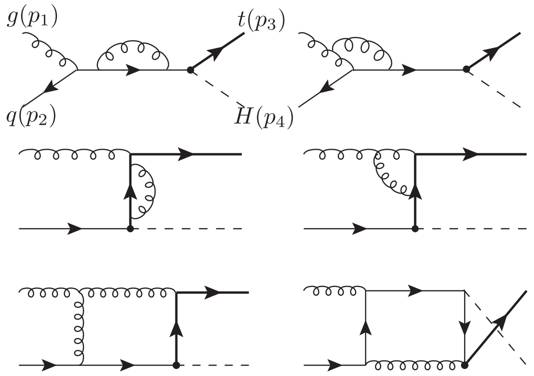

FIG. 2. One-loop virtual Feynman diagrams for the tH associated production via FCNC Htq couplings.

where $C_\epsilon = \Gamma(1+\epsilon)[(4\pi\mu_r^2)/m_t^2]^\epsilon$, μ_r is the renormalization scale, and $n_f = 5$. For the counterterm of FCNC couplings $\delta Z_{g_{qt}}$, we use the modified minimal subtraction ($\overline{\rm MS}$) scheme [33],

$$\delta Z_{g_{qt}} = -\frac{\alpha_s}{4\pi^2}\Gamma(1+\epsilon)(4\pi)^\epsilon\frac{1}{\epsilon_{\rm UV}}, \tag{8}$$

and the running of the FCNC coupling is given by

$$g_{qt}(\mu_r) = g_{qt}(\mu_0)\left(\frac{\alpha_s(\mu_r)}{\alpha_s(\mu_0)}\right)^{4/\beta_0}. \tag{9}$$

Here, $\beta_0 = 11 - \frac{2}{3}n_f$ is the one-loop coefficients of the QCD β function.

In the virtual corrections, the UV divergences are canceled by the counterterms. To deal with IR divergences, we adopt the traditional Passarino-Veltman reduction method to reduce the tensor integrals to scalar integrals [34,35], of which the IR divergences can be obtained by the skill in Ref. [36]. And the IR divergent parts are given by

$$\mathcal{M}^V|_{\rm IR} = \frac{\alpha_s}{2\pi}\frac{\Gamma(1-\epsilon)}{\Gamma(1-2\epsilon)}\left(\frac{4\pi\mu_r^2}{s}\right)^\epsilon\left(\frac{A_2^v}{\epsilon_{\rm IR}^2}+\frac{A_1^v}{\epsilon_{\rm IR}}\right)\mathcal{M}^B, \tag{10}$$

where

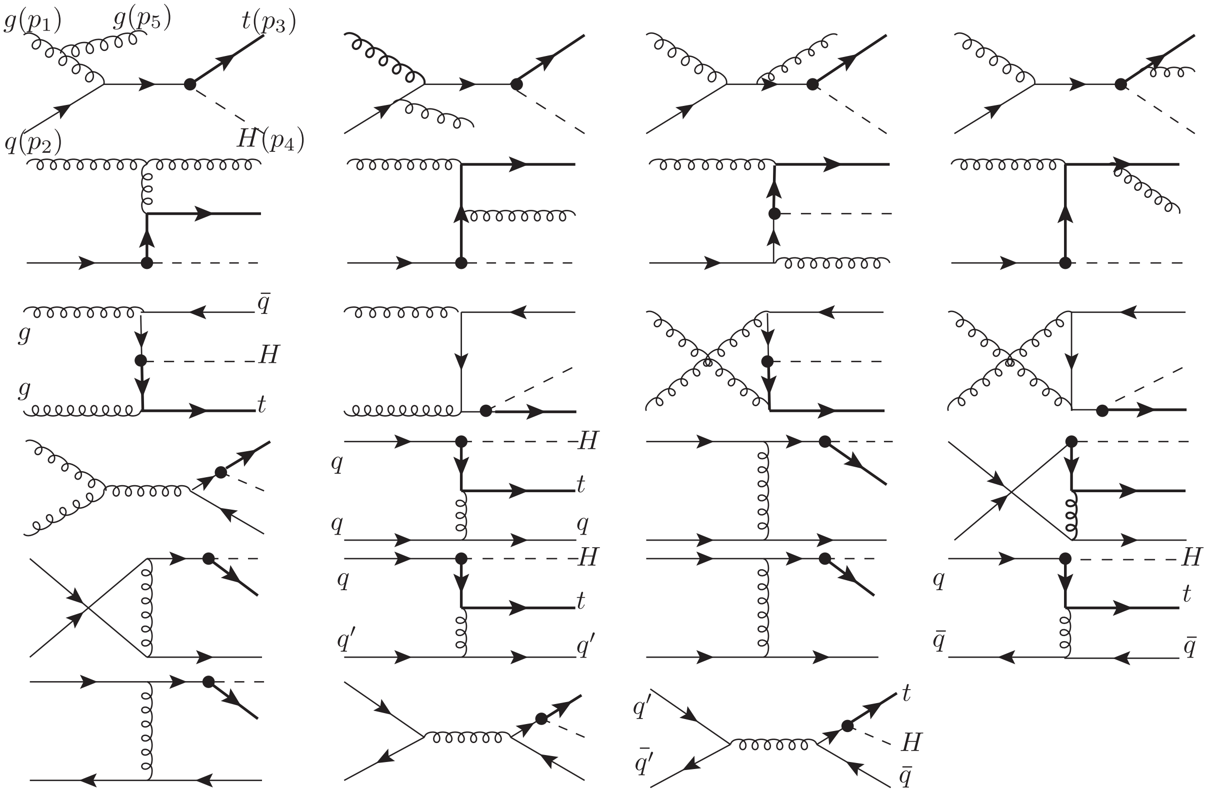

FIG. 3. Feynman diagrams for the real corrections to the tH associated production via FCNC Htq couplings.

$$\begin{aligned} A_2^v &= -\frac{13}{3}, \\ A_1^v &= 3\ln\frac{m_t^2 - t}{m_t^2} - \frac{1}{3}\ln\frac{m_t^2 - u}{m_t^2} - \frac{4}{3}\ln\frac{s}{m_t^2} - \frac{43}{6}. \end{aligned} \tag{11}$$

B. Real corrections

The real corrections contain the radiations of an additional gluon and massless (anti)quark. The relevant Feynman diagrams are shown in Fig. 3. The partonic cross section can be written as

$$\hat{\sigma}^R = \frac{1}{2s}\int dPS^{(3)}\overline{|\mathcal{M}^R|^2}. \tag{12}$$

We use two cutoff phase space slicing methods [32], which introduces two small cutoffs δ_s and δ_c to divide the three-body phase space into three regions. First, the phase space is separated into two regions according to whether or not the energy of the additional gluon satisfies the soft criterion $E_5 \leq \delta_s\sqrt{s}/2$ in the partonic center-of-mass frame. And the partonic cross section can be divided as

$$\hat{\sigma}^R = \hat{\sigma}^{\mathrm{H}} + \hat{\sigma}^S, \tag{13}$$

where $\hat{\sigma}^{\mathrm{H}}$ and $\hat{\sigma}^S$ are the contributions from the hard and the soft regions, respectively. Furthermore, the collinear cutoff δ_c is applied to separate the hard region into two regions according to whether the collinear condition $-\delta_c s < t_{i5} < 0$ is satisfied or not, where $t_{i5} = (p_i - p_5)^2$ with $i = 1, 2$. The corresponding cross section is split into

$$\hat{\sigma}^{\mathrm{H}} = \hat{\sigma}^{\overline{\mathrm{HC}}} + \hat{\sigma}^{\mathrm{HC}}, \tag{14}$$

where the contributions from hard-collinear (HC) regions $\hat{\sigma}^{\mathrm{HC}}$ contain the collinear divergences, and the hard-noncollinear part $\hat{\sigma}^{\overline{\mathrm{HC}}}$ is free of IR singularities and can be calculated numerically.

1. Real gluon emission

In the limit that the energy of the emitted gluon becomes small, i.e., $E_5 \leq \delta_s\sqrt{s}/2$, the amplitude squared $\overline{|\mathcal{M}(qg \to tH + g)|^2}$ can be factorized into the Born amplitude squared and the eikonal factor Φ_{eik},

$$\overline{|\mathcal{M}(qg \to tH + g)|^2} \xrightarrow{\text{soft}} (4\pi\alpha_s\mu_r^{2\epsilon})\overline{|\mathcal{M}^B|^2}\Phi_{\mathrm{eik}}, \tag{15}$$

where the eikonal factor can be expressed as

$$\begin{aligned} \Phi_{\mathrm{eik}} = {}& \frac{C_A}{2}\frac{s}{(p_1 \cdot p_5)(p_2 \cdot p_5)} - \frac{1}{2C_A}\frac{m_t^2 - u}{(p_2 \cdot p_5)(p_3 \cdot p_5)} \\ & + \frac{C_A}{2}\frac{m_t^2 - t}{(p_2 \cdot p_5)(p_3 \cdot p_5)} - C_F\frac{m_t^2}{(p_3 \cdot p_5)^2}, \end{aligned} \tag{16}$$

with $C_A = 3$, $C_F = \frac{4}{3}$. The three-body phase space in the soft region can be factorized into

$$dPS^{(3)}(qg \to tH + g) \xrightarrow{\text{soft}} dPS^{(2)}(qg \to tH)dS, \tag{17}$$

where dS is the integration over the phase space of the soft gluon, given by

$$dS = \frac{1}{2(2\pi)^{3-2\epsilon}}\int_0^{\delta_s\sqrt{s}/2} dE_5 E_5^{1-2\epsilon} d\Omega_{2-2\epsilon}. \tag{18}$$

Hence, the parton level cross section in the soft region can be expressed as

$$\hat{\sigma}^S = (4\pi\alpha_s\mu_r^{2\epsilon})\hat{\sigma}^B\int \Phi_{\mathrm{eik}} dS. \tag{19}$$

After integration over the soft phase space, Eq. (19) becomes

$$\hat{\sigma}^S = \hat{\sigma}^B\left[\frac{\alpha_s}{2\pi}\frac{\Gamma(1-\epsilon)}{\Gamma(1-2\epsilon)}\left(\frac{4\pi\mu_r^2}{s}\right)^{\epsilon}\right]\left(\frac{A_2^s}{\epsilon_{\mathrm{IR}}^2} + \frac{A_1^s}{\epsilon_{\mathrm{IR}}} + A_0^s\right), \tag{20}$$

with

$$\begin{aligned} A_2^s &= \frac{13}{3}, \\ A_1^s &= -2A_2^s\ln\delta_s + \frac{1}{3}\ln\frac{m_t^2 - u}{m_t^2} - 3\ln\frac{m_t^2 - t}{m_t^2} + \frac{4}{3}\ln\frac{s}{m_t^2} + \frac{4}{3}, \\ A_0^s &= -2A_2^s\ln^2\delta_s - 2A_1^s\ln\delta_s + \frac{4}{3\beta}\ln\frac{1+\beta}{1-\beta} + \frac{3}{2}B_- - \frac{1}{6}B_+. \end{aligned} \tag{21}$$

The $B_\pm$ are defined as

$$\begin{aligned} B_\pm = {}& \ln^2\frac{1-\beta}{1 \pm \beta\cos\theta} - \frac{1}{2}\ln^2\frac{1+\beta}{1-\beta} \\ & + 2\mathrm{Li}_2\left[\frac{\mp\beta(\cos\theta \pm 1)}{1-\beta}\right] - 2\mathrm{Li}_2\left[\frac{\pm\beta(\cos\theta \mp 1)}{1 \pm \beta\cos\theta}\right], \end{aligned} \tag{22}$$

where $\beta = \sqrt{1 - 4m_t^2 s/(m_t^2 - m_H^2 + s)^2}$ and $\cos\theta = (t-u)/\sqrt{(m_t^2 - m_h^2 + s)^2 - 4m_t^2 s}$.

In the hard-collinear region, collinear singularities arise when the emitted hard gluon is collinear to the incoming massless partons. As the conclusion of the factorization theorem [37,38], the amplitude squared $\overline{|\mathcal{M}(qg \to tH + g)|^2}$ can be factorized into the product of the Born amplitude squared and the Altarelli-Parisi splitting function; that is

$$\begin{aligned} & \overline{|\mathcal{M}(qg \to tH + g)|^2} \xrightarrow{\text{coll}} (4\pi\alpha_s\mu_r^{2\epsilon})\overline{|\mathcal{M}^B|^2} \\ & \quad \times \left(\frac{-2P_{gg}(z,\epsilon)}{zt_{15}} + \frac{-2P_{qq}(z,\epsilon)}{zt_{25}}\right), \end{aligned} \tag{23}$$

where z denotes the fraction of the momentum of the incoming parton carried by $q(g)$. The unregulated

Altarelli-Parisi splitting functions are written explicitly as [32]

$$
\begin{aligned}
P_{qq}(z,\epsilon) &= C_F\left(\frac{1+z^2}{1-z}-\epsilon(1-z)\right),\\
P_{gg}(z,\epsilon) &= 2C_A\left(\frac{z}{1-z}+\frac{1-z}{z}+z(1-z)\right).
\end{aligned}
\tag{24}
$$

Then we factorize the three-body phase space in the collinear limit $-\delta_c s < t_{i5} < 0$ as

$$
\begin{aligned}
dPS^{(3)}(qg\to tH+g)\xrightarrow{\text{coll}} dPS^{(2)}(qg\to tH; s'=zs)\\
\times\frac{(4\pi)^{\epsilon}}{16\pi^2\Gamma(1-\epsilon)}dz dt_{i5}\\
\times[-(1-z)t_{i5}]^{-\epsilon}.
\end{aligned}
\tag{25}
$$

Thus, after convoluting with the PDFs, the three-body cross section in the hard-collinear region can be written as [32]

$$
\begin{aligned}
\sigma^{\mathrm{HC}} = \int dx_1dx_2\hat{\sigma}^{B}_{qg}\left[\frac{\alpha_s}{2\pi}\frac{\Gamma(1-\epsilon)}{\Gamma(1-2\epsilon)}\left(\frac{4\pi\mu_r^2}{s}\right)^{\epsilon}\right]\\
\times\left(-\frac{1}{\epsilon}\right)\delta_c^{-\epsilon}[P_{qq}(z,\epsilon)G_{q/p}(x_1/z)G_{g/p}(x_2)\\
+P_{gg}(z,\epsilon)G_{g/p}(x_2/z)G_{q/p}(x_1)\\
+(x_1\leftrightarrow x_2)]\frac{dz}{z}\left(\frac{1-z}{z}\right)^{-\epsilon},
\end{aligned}
\tag{26}
$$

where $G_{q(g)/p}(x)$ is the bare PDF.

2. Massless (anti)quark emission

In addition to the real gluon emission, an additional massless $q(\bar{q})$ in the final state should be taken into consideration at $\mathcal{O}(\alpha_s)$ of the perturbative expansion. Since the contributions from real massless $q(\bar{q})$ emission contain initial-state collinear singularities, we need to use the two cutoff phase space slicing method [32] to isolate these collinear divergences. The cross section for the process with an additional massless $q(\bar{q})$ emission, including the noncollinear part and collinear part, can be expressed as

$$
\begin{aligned}
\sigma^{\mathrm{add}} = \int dx_1dx_2\sum_{(\alpha=q,\bar{q},q')}\Bigg\{\hat{\sigma}^{\bar{C}}(q\alpha\to tH+q(\bar{q}))G_{q/p}(x_1)G_{\alpha/p}(x_2)+\hat{\sigma}^{B}_{qg}\left[\frac{\alpha_s}{2\pi}\frac{\Gamma(1-\epsilon)}{\Gamma(1-2\epsilon)}\left(\frac{4\pi\mu_r^2}{s}\right)^{\epsilon}\right]\\
\times\left(-\frac{1}{\epsilon}\right)\delta_c^{-\epsilon}P_{g\alpha}(z,\epsilon)G_{q/p}(x_1)G_{\alpha/p}(x_2/z)\frac{dz}{z}\left(\frac{1-z}{z}\right)^{-\epsilon}+(x_1\leftrightarrow x_2)\Bigg\}\\
+\int dx_1dx_2\Bigg\{\hat{\sigma}^{\bar{C}}(gg\to tH+\bar{q})G_{g/p}(x_1)G_{g/p}(x_2)+\hat{\sigma}^{B}_{qg}\left[\frac{\alpha_s}{2\pi}\frac{\Gamma(1-\epsilon)}{\Gamma(1-2\epsilon)}\left(\frac{4\pi\mu_r^2}{s}\right)^{\epsilon}\right]\\
\times\left(-\frac{1}{\epsilon}\right)\delta_c^{-\epsilon}P_{qg}(z,\epsilon)G_{g/p}(x_1/z)G_{g/p}(x_2)\frac{dz}{z}\left(\frac{1-z}{z}\right)^{-\epsilon}+(x_1\leftrightarrow x_2)\Bigg\},
\end{aligned}
\tag{27}
$$

where

$$
\begin{aligned}
P_{qg}(z,\epsilon) &= P_{\bar{q}g}(z) = \frac{1}{2}\left[z^2+(1-z)^2\right]-z(1-z)\epsilon,\\
P_{gq}(z,\epsilon) &= P_{g\bar{q}}(z) = C_F\left[\frac{z}{1+(1-z)^2}-z\epsilon\right].
\end{aligned}
\tag{28}
$$

The $\hat{\sigma}^{\bar{C}}$ is the noncollinear cross sections for the processes of the $q\bar{q}(q,q')$, gg, and $q'\bar{q}'$ initial states,

$$
\begin{aligned}
\hat{\sigma}^{\bar{C}} = \frac{1}{2s}\int\Bigg\{\sum_{(\alpha=q,\bar{q},q')}|\mathcal{M}(q\alpha\to tH+\alpha)|^2\\
+|\mathcal{M}(gg\to tH+\bar{q})|^2+|\mathcal{M}(q'\bar{q}'\to tH+\bar{q})|^2\Bigg\}dPS^{(3)}_{\bar{C}},
\end{aligned}
\tag{29}
$$

in which $dPS^{(3)}_{\bar{C}}$ is the three-body phase space in the noncollinear region.

3. Mass factorization

There are still collinear divergences in the partonic cross sections after adding the renormalized virtual corrections and the real corrections. The remaining divergences can be factorized into a redefinition of the PDFs. In the $\overline{\mathrm{MS}}$ convention, the scale-dependent PDF $G_{\alpha/p}(x,\mu_f)$ can be written as [32]

$$
\begin{aligned}
G_{\alpha/p}(x,\mu_f)\\
= G_{\alpha/p}(x)+\sum_{\beta}\left(-\frac{1}{\epsilon}\right)\left[\frac{\alpha_s}{2\pi}\frac{\Gamma(1-\epsilon)}{\Gamma(1-2\epsilon)}\left(\frac{4\pi\mu_r^2}{\mu_f^2}\right)^{\epsilon}\right]\\
\times\int_x^1\frac{dz}{z}P_{\alpha\beta}(z)G_{\beta/p}(x/z).
\end{aligned}
\tag{30}
$$

The Altarelli-Parisi splitting function is defined by

$$
P_{\alpha\beta}(y,\epsilon) = P_{\alpha\beta}(y)+\epsilon P'_{\alpha\beta}(y).
\tag{31}
$$

The resulting $\mathcal{O}(\alpha_s)$ expression for the initial-state collinear contribution can be written in the following form:

$$
\begin{aligned}
\sigma^{\mathrm{coll}} = \int dx_1 dx_2 \hat{\sigma}^B_{qg}\bigg[\frac{\alpha_s}{2\pi}\frac{\Gamma(1-\epsilon)}{\Gamma(1-2\epsilon)}\bigg(\frac{4\pi\mu_r^2}{s}\bigg)^{\epsilon}\bigg] \\
\times\bigg\{\tilde{G}_{q/p}(x_1,\mu_f)G_{g/p}(x_2,\mu_f) \\
+ G_{q/p}(x_1,\mu_f)\tilde{G}_{g/p}(x_2,\mu_f) \\
+ \sum_{\alpha=q,g}\bigg[\frac{A_1^{\mathrm{sc}}(\alpha\to\alpha g)}{\epsilon} + A_0^{\mathrm{sc}}(\alpha\to\alpha g)\bigg] \\
\times G_{q/p}(x_1,\mu_f)G_{g/p}(x_2,\mu_f) + (x_1\leftrightarrow x_2)\bigg\}, \qquad (32)
\end{aligned}
$$

where

$$
\begin{aligned}
A_1^{\mathrm{sc}}(q\to qg) &= C_F\bigg(2\ln\delta_s + \frac{3}{2}\bigg), \\
A_1^{\mathrm{sc}}(g\to gg) &= 2C_A\ln\delta_s + \frac{11C_A - 2n_f}{6}, \qquad (33) \\
A_0^{\mathrm{sc}} &= A_1^{\mathrm{sc}}\ln\bigg(\frac{s}{\mu_f^2}\bigg),
\end{aligned}
$$

and

$$
\tilde{G}_{\alpha/p}(x,\mu_f) = \sum_{\beta}\int_x^{1-\delta_s\delta_{\alpha\beta}}\frac{dy}{y}G_{\beta/p}\bigg(\frac{x}{y},\mu_f\bigg)\tilde{P}_{\alpha\beta}(y), \qquad (34)
$$

with

$$
\tilde{P}_{\alpha\beta}(y) = P_{\alpha\beta}(y)\ln\bigg(\delta_c\frac{1-y}{y}\frac{s}{\mu_f^2}\bigg) - P'_{\alpha\beta}(y). \qquad (35)
$$

Finally, we combine all of the results above to give the NLO total cross section for the $pp\to tH$ process:

$$
\begin{aligned}
\sigma^{\mathrm{NLO}} = \int dx_1 dx_2\{[G_{q/p}(x_1,\mu_f)G_{g/p}(x_2,\mu_f) + x_1\leftrightarrow x_2] \\
\times(\hat{\sigma}^B + \hat{\sigma}^V + \hat{\sigma}^S + \hat{\sigma}^{\overline{\mathrm{HC}}})\} + \sigma^{\mathrm{coll}} \\
+ \sum_{(\alpha,\beta)}\int dx_1 dx_2[G_{\alpha/p}(x_1,\mu_f)G_{\beta/p}(x_2,\mu_f) \\
+ (x_1\leftrightarrow x_2)]\hat{\sigma}^{\bar{C}}(\alpha\beta\to tH+X), \qquad (36)
\end{aligned}
$$

where (α,β) stand for the $q\bar{q}(q,q')$, gg, and $q'\bar{q}'$ initial states. Note that there contain no singularities any more, since $A_2^v + A_2^s = 0$ and $A_1^v + A_1^s + A_1^{\mathrm{sc}}(q\to qg) + A_1^{\mathrm{sc}}(g\to gg) = 0$.

IV. PRODUCTION CROSS SECTION

In this section, we give the numerical results for the total and differential cross sections for the Higgs boson and the top quark associated production via the FCNC Htq couplings.

A. Experiment Constraints

Before proceeding, we discuss the choice of the FCNC Htq couplings, which is constrained by low-energy data on the flavor-mixing process. For example, in the precision measurement of the magnetic dipole moments of the proton and the neutron, the contribution of the g_{ut} vertex should be less than the experimental uncertainty [25,26]. The result reveals that $\mathrm{Im}(g^a_{qt})$ is more strongly suppressed than $\mathrm{Re}(g^v_{ut})$. Therefore, the FCNC Htq coupling can be described by only one real parameter, i.e., the strength of the coupling g_{qt}, which is constrained as

$$
\bigg(\frac{g}{2\sqrt{2}}g_{ut}\bigg)^2 < 54\pi^2\frac{\Delta a_p^{\mathrm{Exp}}}{x_t x_p g(x_t)}, \qquad (37)
$$

where

$$
g(x) = \frac{3 + x^2(x^2-4) + 2\log(x^2)}{2(x^2-1)^3}, \qquad (38)
$$

with $x_a = m_a/m_H$.

In D^0-$\bar{D}^0$ mixing, the g_{ut} and g_{ct} couplings can contribute to the mass difference ΔM_D through loop effects. Experiment results impose limits on g_{ut} and g_{ct} as [25,26]

$$
|g_{ut}g_{ct}| < \frac{1.73\times 10^{-2}}{\sqrt{f(x) - 2g(x)}}, \qquad (39)
$$

where

$$
\begin{aligned}
f(x) &= \frac{1}{2}\frac{1}{(1-x)^3}(1 - x^2 + 2x\log x), \qquad (40) \\
g(x) &= \frac{4}{(1-x)^3}(2(1-x) + (1+x)\log x),
\end{aligned}
$$

with $x = m_H^2/m_t^2$.

The EW precision observables Γ_Z, R_c, R_b,R_l, A_c and A^c_{FB} also impose constraints on the couplings g_{ct} through the radiative corrections to the effective $Zc\bar{c}$ vertex [27]. In Table I, we list the 95% C.L. upper limits on the FCNC Htq couplings obtained from the low-energy experiments.

B. Cross sections at the LHC

Now we discuss the numerical results of the Higgs boson and the top quark associated production at the LHC. Unless specified otherwise, we choose $g_{ut} = 0.2$ and $g_{ct} = 0.2$, which are allowed by the low-energy experiments. We

TABLE I. The 95% C.L. upper limits on the FCNC Htq couplings obtained from the low-energy experiments, with Higgs boson mass in the range from 115 to 170 GeV.

Couplings	Upper limits	Experiments
g_{ut}	$0.363\sim 0.393$	magnetic dipole moments [25]
$g_{ut}g_{ct}$	$0.0194\sim 0.0272$	D^0-$\bar{D}^0$ mixing [25]
g_{ct}	$0.270\sim 0.319$	$Z\to c\bar{c}$ [27]

have checked that the imaginary part of these couplings does not contribute to the final results, so $\mathrm{Im}(g^a_{qt})$ is neglected in numerical calculations. Other SM input parameters are

$$\begin{aligned} m_t &= 173.1\ \mathrm{GeV}, & m_H &= 125\ \mathrm{GeV}, \\ m_W &= 80.398\ \mathrm{GeV}, & m_b(m_b) &= 4.2\ \mathrm{GeV}, \\ \alpha &= 1/127.921, & \sin^2\theta_W &= 0.2312, \\ && \alpha_s(m_Z) = 0.118. && \end{aligned} \tag{41}$$

The CTEQ6L (CTEQ6M) PDF sets and the corresponding running QCD coupling constant α_s are used in the LO (NLO) calculations. The factorization and renormalization scales are set as $\mu_f = \mu_r = \mu_0$, and $\mu_0 = m_t + m_H$. Moreover, as to the Yukawa couplings of the bottom quark, we take the running mass $m_b(Q)$ evaluated by the NLO formula [39]

$$m_b(Q) = U_6(Q, m_t)U_5(m_t, m_b)m_b(m_b). \tag{42}$$

The evolution factor U_f is given by

$$U_f(Q_2, Q_1) = \left(\frac{\alpha_s(Q_2)}{\alpha_s(Q_1)}\right)^{d^{(n_f)}}\left[1 + \frac{\alpha_s(Q_1) - \alpha_s(Q_2)}{4\pi}J^{(n_f)}\right], \tag{43}$$

with

$$d^{(n_f)} = \frac{12}{33 - 2n_f}, \qquad J^{(n_f)} = -\frac{8982 - 504n_f + 40n_f^2}{3(33 - 2n_f)^2}. \tag{44}$$

In Fig. 4, we show the dependence of the NLO cross sections on the cutoffs δ_s and δ_c. In fact, the soft-collinear and the hard-noncollinear parts individually strongly depend on the cutoffs. But the total cross section is independent on cutoffs after all pieces are added together. From Fig. 4, we can see that the change of σ^{NLO} is very slow for δ_s in the range from 10^{-6} to 10^{-2}, which indicates that it is reasonable to use the two cutoff phase space slicing method.

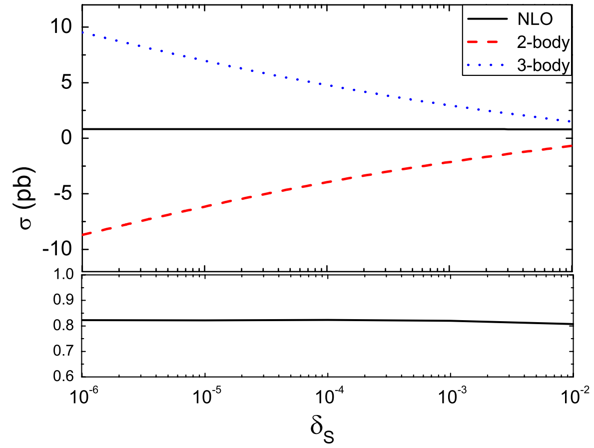

FIG. 4 (color online). Dependence of the NLO total cross sections at the LHC on the cutoff scale δ_s with $\delta_c = \delta_s/50$. The label two body represents the LO cross section, the one-loop virtual corrections, the soft- and hard-collinear limits of the cross sections of three-body final states, while the label three body denotes the cross sections of hard-noncollinear part.

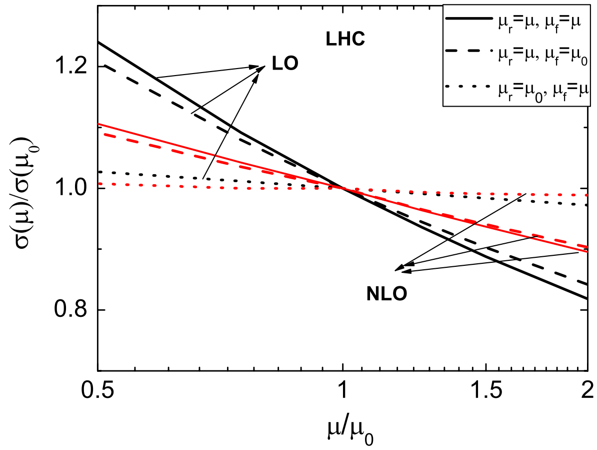

FIG. 5 (color online). Scale dependences of the cross sections for the gu initial-state subprocess at the LHC.

In Fig. 5, we give the scale dependences of the LO and NLO total cross sections. Explicitly, we consider three cases: (1) factorization scale dependence ($\mu_r = \mu_0$ and $\mu_f = \mu$), (2) renormalization scale dependence ($\mu_f = \mu_0$ and $\mu_r = \mu$), and (3) total scale dependences ($\mu_f = \mu_r = \mu$). From Fig. 5, we find that the NLO corrections significantly reduce the scale dependences for all three cases, which makes the theoretical predictions more reliable.

Figure 6 presents the dependence of the total cross sections on m_H. It can be seen that the cross sections

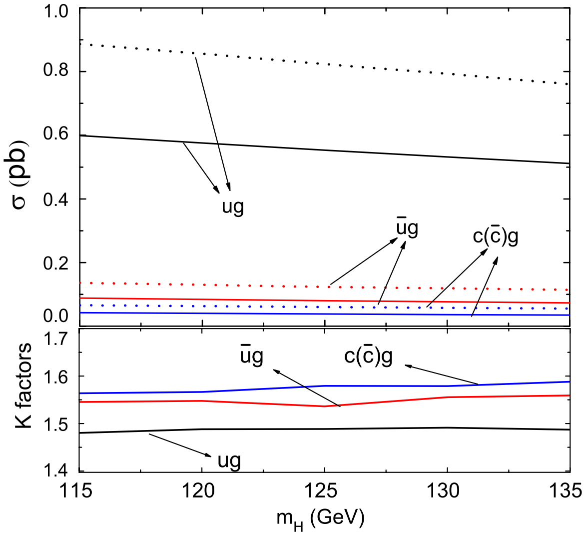

FIG. 6 (color online). The LO and NLO total cross sections and K factors as functions of m_H. The solid lines and the dotted lines represent the LO and NLO cross sections, respectively.

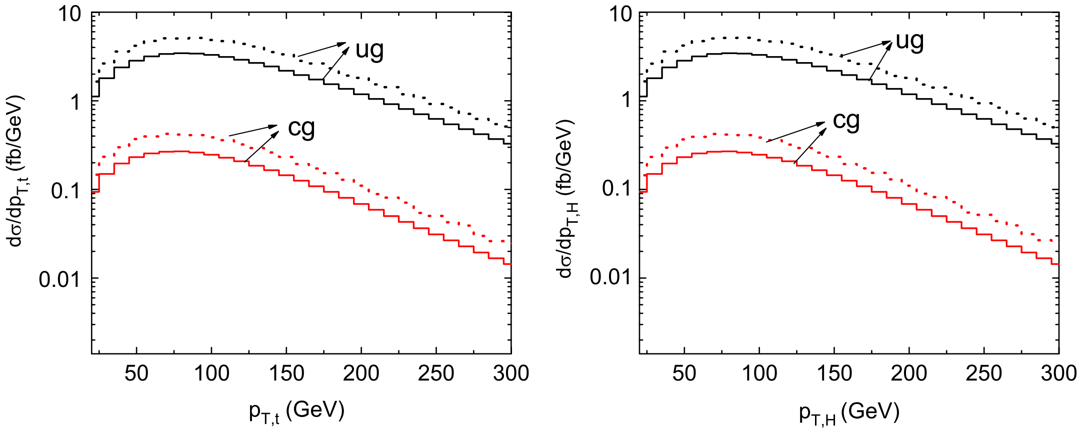

FIG. 7 (color online). The transverse momentum distributions of the top quark and the Higgs boson at the LHC. The solid line and the dotted line represent the LO and the NLO results, respectively.

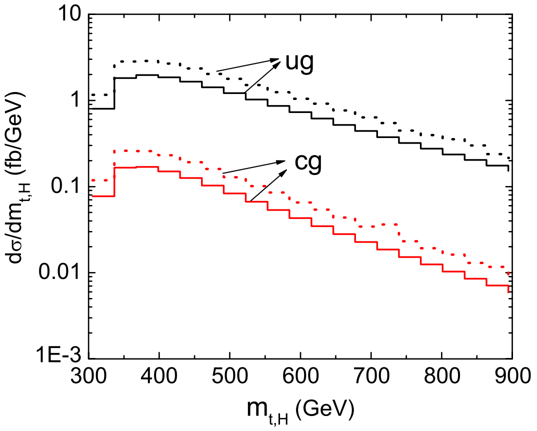

FIG. 8 (color online). Distributions of the invariant mass of the top quark and Higgs boson. The solid line and the dotted line represent the LO and the NLO results, respectively.

decrease by about 16% as m_H increases from 115 to 135 GeV. In Fig. 6, the K factors, defined as $\sigma^{\rm NLO}/\sigma^{\rm LO}$, are also shown. We can see that the K factors for $ug \to tH$, $\bar u g \to \bar t H$ and $c(\bar c)g \to tH$ processes are 1.49, 1.54, and 1.58, respectively, at the LHC for $m_H = 125$ GeV, and they are not sensitive to the Higgs boson mass.

Figure 7 shows the differential cross sections as a function of the transverse momentum of the top quark and the Higgs boson. We find that they are very similar and the peak positions are around 80 GeV. In Fig. 8, we present the distributions of the invariant mass of the top quark and Higgs boson, and the peaks are around 360 GeV. From these figures, we can see that the NLO corrections significantly increase the LO results, but do not change the distribution shapes.

V. SIGNAL AND DISCOVERY POTENTIALITY

In this section, we investigate the signal and corresponding backgrounds in detail and present the discovery potential of the signal of the tH associated production at the LHC.

A. NLO prediction on FCNC *tH* associated production and decay

We have discussed the QCD NLO corrections to tH associated production in the last section. In order to provide a complete QCD NLO prediction on the signal, we need to include the QCD NLO corrections to the decay of the top quark and the Higgs boson. In this work, we concentrate on the top quark semileptonic decay and the Higgs boson decaying to $b\bar b$, as shown in Fig. 9.

The complete NLO cross section for tH associated production and decay can be written as

$$\sigma^{\rm NLO}(pp \to t(\to \nu_l l^+ b) + H(\to b\bar b)) = (\sigma_0 + \alpha_s \alpha_1) \times \left(\frac{\delta\Gamma_0^H + \alpha_s \delta\Gamma_1^H}{\Gamma_0^H + \alpha_s \Gamma_1^H}\right)\left(\frac{\delta\Gamma_0^t + \alpha_s \delta\Gamma_1^t}{\Gamma_0^t + \alpha_s \Gamma_1^t}\right), \tag{45}$$

where σ_0 is the LO contribution to the tH associated production rate; Γ_0^t, Γ_0^H are the LO total top quark and Higgs boson decay width; and $\delta\Gamma_0^t$, $\delta\Gamma_0^H$ are the decay width of the top quark decaying into $\nu_l l^+ b$ and the Higgs boson decaying into $b\bar b$. $\alpha_s\sigma_1$, $\alpha_s\Gamma_1^i$, and $\alpha_s\delta\Gamma_1^i$, with $i = t$, H, are the corresponding NLO corrections. We choose $\Gamma_0^H = 3.28\times10^{-3}$ GeV, $\alpha_s\Gamma_1^H = 4.07\times10^{-3}$ GeV.

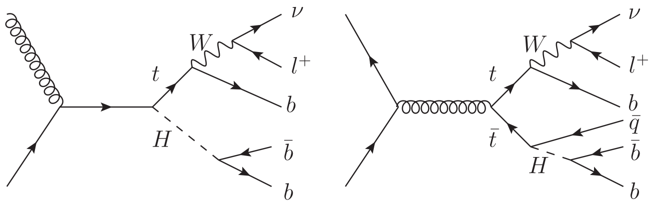

FIG. 9. Representative Feynman diagrams for tH production and $t\bar t \to tH\bar q$ production via FCNC Htq couplings.

And we calculate the width of the Higgs boson by Bridge at the LO [40], and adopt NLO results in Ref. [41]. Here we use the modified narrow width approximation (MNW) incorporating the finite width effects as the treatment in Refs. [42,43].

We expand Eq. (45) to order α_s,

$$\begin{aligned}\sigma^{\mathrm{NLO}} &= \sigma_0 \times \frac{\delta\Gamma_0^t}{\Gamma_0^t}\frac{\delta\Gamma_0^H}{\Gamma_0^H} + \alpha_s\sigma_1 \times \frac{\delta\Gamma_0^t}{\Gamma_0^t}\frac{\delta\Gamma_0^H}{\Gamma_0^H} \\ &\quad + \sigma_0 \times \frac{\alpha_s\delta\Gamma_1^t}{\Gamma_0^t}\frac{\delta\Gamma_0^H}{\Gamma_0^H} - \sigma_0 \times \frac{\delta\Gamma_0^t}{\Gamma_0^t}\frac{\alpha_s\Gamma_1^t}{\Gamma_0^t}\frac{\delta\Gamma_0^H}{\Gamma_0^H} \\ &\quad + \sigma_0 \times \frac{\alpha_s\delta\Gamma_1^H}{\Gamma_0^H}\frac{\delta\Gamma_0^t}{\Gamma_0^t} - \sigma_0 \times \frac{\delta\Gamma_0^H}{\Gamma_0^H}\frac{\alpha_s\Gamma_1^H}{\Gamma_0^H}\frac{\delta\Gamma_0^t}{\Gamma_0^t} \\ &\quad + \mathcal{O}(\alpha_s^2). \end{aligned} \tag{46}$$

Now we can separate QCD NLO corrections into three classes, i.e., the tH associated production at the NLO with subsequent decay at the LO, production at the LO with subsequent decay at the NLO, and production and decay at the LO but having NLO corrections from MNW. We note that QCD NLO corrections to the top quark decay part will contribute little since the branching ratio of the top quark decaying into W boson is always 100% [44]. As a consequence, the third term and the fourth term of Eq. (46) almost cancel each other. Since we only consider one decay mode of Higgs bosons, the sum of the fifth term and the sixth term will give a negative contribution.

There is another process, which is at the same order as the tH associated production at the NLO [Fig. 9 (right)], i.e., $t\bar{t}$ production with the top quark semilepton decay and the antitop decaying into $H\bar{q}$ via the FCNC vertex. It has the same signal if the light quark from the top quark is missed by the detector. This additional contribution is very significant for detecting the g_{ct} couplings, because the $cg \to tH$ process is suppressed by the c quark PDF.

B. Collider simulation

To account for the resolution of the detectors, we apply energy and momentum smearing effects to the final states [45],

$$\begin{aligned} \Delta E_l/E_l &= 0.05/\sqrt{E_l/\mathrm{GeV}} \oplus 0.0055, \\ \Delta E_{b(j)}/E_{b(j)} &= 1/\sqrt{E_{b(j)}/\mathrm{GeV}} \oplus 0.05, \end{aligned} \tag{47}$$

where $E_{l,b,j}$ are the energy of the lepton, b-jet, and the other jets, respectively.

We use the anti-k_t jet algorithm [46] with the jet radius $R = 0.4$ and require the final-state particle to satisfy the following basic kinematic cuts:

$$\begin{aligned} &p_{T_l} > 25~\mathrm{GeV}, \qquad \not{E}_T > 25~\mathrm{GeV}, \qquad p_{T_{b,j}} > 25~\mathrm{GeV}, \\ &|\eta_l| < 2.5, \qquad |\eta_{b,j}| < 2.5, \qquad \Delta R_{bl,jl,bj} > 0.4. \end{aligned} \tag{48}$$

Here $\not{E}_T$ is the missing transverse energy. $p_{T_{b,j,l}}$ and $\eta_{b,j,l}$ are the transverse momentum and pseudorapidity of the b jet, other quark jets, and leptons, respectively. And $\Delta R = \sqrt{(\Delta\eta)^2 + (\Delta\phi)^2}$ stands for the angular distance. Moreover, we choose a b-tagging efficiency of 0.6 for b jets and mistagging rates of 1% for other quarks.

C. Events selection

The main background arises from the $t\bar{t}$ production with one top quark leptonic decay and the other top quark hadronic decay. Other backgrounds include $Wbbj$, WZj, and $Wjjj$ production processes. These backgrounds are calculated at the LO by using the MADGRAPH4 [47] and ALPGEN [48] programs.

For the signal, we require three tagged b jets, $b^{1,2,3}$, a lepton l^+ and the missing energy in the final states at both LO and NLO. When considering the number and kind of the final-state jets after jet clustering, there are several cases as follows:

1. Fewer than three exclusive b jets where two b jets are combined together. We discard such events.
2. Three exclusive b jets. It can be from the LO and virtual corrections, which have three bottom quarks in the final states. The final states of real corrections can also give three b jets if the additional emitted parton is combined into one of the b jets. As a result, some combination procedure of jets may be different from the real partonic process. For example, the additional gluon comes from the initial states or the top quark decay, but it is combined into the b jets arising from the Higgs boson, which will change the reconstructed particle mass spectrum.
3. Four exclusive jets where the additional jet comes from a gluon or light quark. We only use the three tagged b jets, neglecting the additional jet, in the final states to reconstruct the top quark and the Higgs boson. If the additional jet comes from the decay process, the reconstructed particle mass will be lower than the exact value due to lack of the momentum of the additional jet.
4. Four exclusive jets where the additional jet comes from a $b(\bar{b})$ quark. If all of these jets are tagged, we must distinguish which one is the additional jet. But the cross section for such a process is strongly suppressed by the $b(\bar{b})$ quark PDF, this contribution is neglectable.

The momentum of neutrino can be obtained by solving the on shell mass-energy equation of the W boson

$$(p_l + p_{\nu,T} + p_{\nu,L})^2 = m_{W,r}^2, \tag{49}$$

where p_l is the momentum of the lepton, and $m_{W,r}$ is the reconstructed W boson mass. We denote the longitudinal and transverse momentum of the neutrino as $p_{\nu,L}$ and $p_{\nu,T}$, respectively. Since we generate intermediated particles with the MNW method, the masses of the intermediated particles change with Breit-Weinger distribution in a region of twenty times their widths around the central value set in Eq. (41). At the same time, smearing effects on the final-state particles also affect the reconstructed W mass. As a result, if we choose a low mass of W boson, there may be no solution for $p_{\nu,L}$ in Eq. (49). So we must estimate a W boson mass, which is large enough to provide the solution of the mass-energy equation and small enough to reconstruct the proper top quark mass. Since there are three b jets in the final states, it is necessary to determine the proper combination of the b jets to reconstruct the top quark mass $m_{t,r}$ and the Higgs boson mass $m_{H,r}$. In practice, we adopt the following steps:

(i) We choose $m_{W,r}$ randomly with Breit-Weinger distribution when solving Eq. (49) to get the neutrino longitudinal momentum. For such $m_{W,r}$, it is required to provide real solutions of the equation. If not, discard this value of $m_{W,r}$ and redo this step until we obtain real solutions.

(ii) In order to improve the W boson reconstruction efficiency and save calculation time, we repeat step 1 ten times and denote the solutions as $p^{i,j}_{\nu,L}$, with $i = 1, 2$, $j = 1, \cdots, 10$. The superscript i represents the number of the solutions in Eq. (49).

(iii) Choose one momentum of the b jets p^k_b, $k = 1, 2, 3$ and one of $p^{i,j}_{\nu,L}$ to reconstruct the top quark mass $m^{i,j,k}_{t,r} = \sqrt{(p_l)^2 + (p^{i,j}_{\nu,L})^2 + (p_{\nu,T})^2 + (p^k_b)^2}$.

(iv) For all combinations of (i, j, k), we choose the best one to minimize $|m^{i,j,k}_{t,r} - m_t|$.

(v) Use the remnant b jets to reconstruct Higgs boson mass $m^k_{H,r}$.

In order to choose appropriate kinematic cuts, we show some important kinematic distributions for the signal and the backgrounds. In Fig. 10, we present dependence of differential cross sections of the signal and backgrounds on H_T, defined as the scalar sum of lepton and jet transverse momenta. From the figure, we can see that the distributions of $Wjjj$, WZj, and $Wbbj$ backgrounds have peaks below 200 GeV, while the peak positions of the signals are about 240 GeV. Therefore, we choose the H_T cut

$$H_T > 200\ \text{GeV}. \tag{50}$$

Figure 11 illustrates the distribution of the reconstructed Higgs boson mass of the signal and backgrounds. We can see that the signals have peaks around 125 GeV, while the distributions of backgrounds are continuous or have peaks at other places. In order to suppress $Wbbj$, WZj, and $Wjjj$ backgrounds, we require the mass of the Higgs boson to satisfy

$$\Delta m_{H,r} < 20\ \text{GeV}, \tag{51}$$

where $\Delta m_{H,r}$ is defined as $|m_{H,r} - m_H|$. The reason will be explained in more detail in the Appendix. We also show the distribution of the reconstructed top quark mass in Fig. 11, where the signal and the backgrounds have similar distributions. As a result, we choose the cut

$$\Delta m_{t,r} < \ 20\ \text{GeV} \tag{52}$$

to keep more signal events, where $\Delta m_{t,r}$ is defined as $|m_{t,r} - m_t|$.

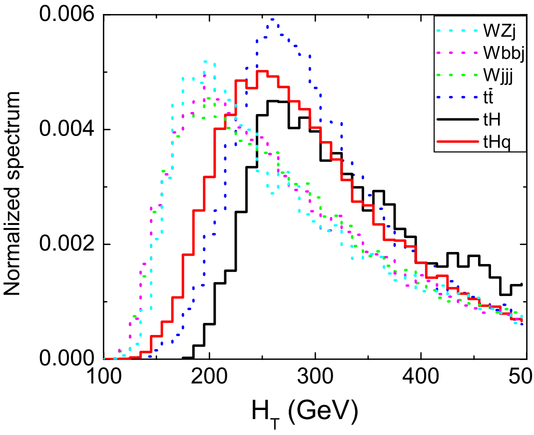

FIG. 10 (color online). Dependence of differential cross sections on H_T. The label tH represents the tH associated production, while the label tHq stands for the process of $t\bar{t}$ production with rare decay mode $t\bar{t} \to tH\bar{q}$. The other labels denote the backgrounds.

To determine the rapidity cut, we present the normalized spectrum of the rapidity of the reconstructed resonances for the signal and backgrounds in Fig. 12. It can be seen that the Higgs boson from the $ug \to tH$ associated production concentrates in the forwards and backwards regions. This is due to the fact that the momentum of initial u quark is generally larger than that of the gluon, so the partonic center-of-mass frame is highly boosted along the direction of the u quark. On the contrary, the main contribution of top pair production comes from gluon initial states, which are symmetric and have small boost effect. So we impose rapidity cut on reconstructed Higgs boson for the signal of $ug \to tH$ process as

$$|y_{H,r}| > 1.0. \tag{53}$$

However, since the c quark is the sea quark, the momentum of the nitial c quark is much smaller than that of the initial u quark. As a result, the Higgs boson from cg initial states is not boosted as from ug initial states. In addition, the cross section of $t\bar{t} \to tH\bar{c}$ decay is comparable to that of $cg \to tH$ process. Therefore, when discussing the Htc couplings, we do not apply the cut in Eq. (53).

The complete set of kinematical cuts is listed in Table II.

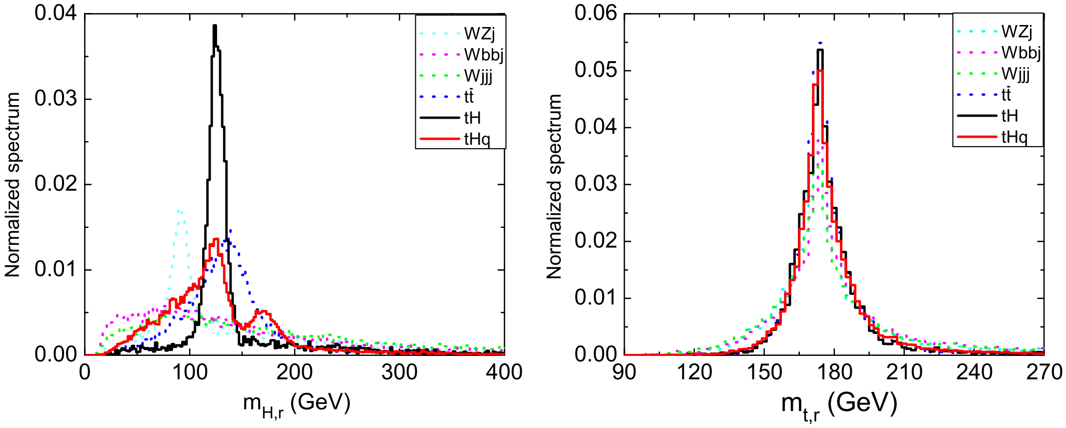

FIG. 11 (color online). The reconstructed top quark and Higgs boson mass. The labels here are the same as those in Fig. 10.

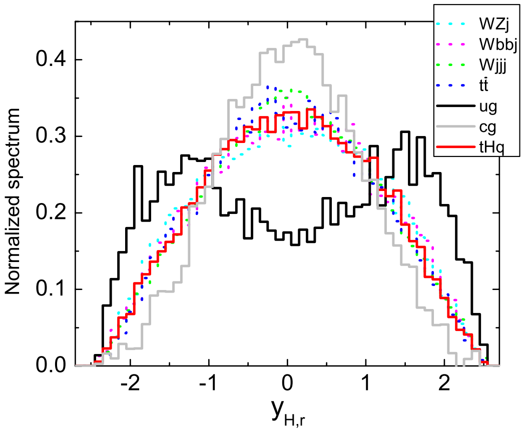

FIG. 12 (color online). Dependence of differential cross sections on the rapidity of the Higgs boson and the top quark. The labels $u(c)g$ represent the $u(c)g \to tH$ associated productions, while the label tHq stands for the process of $t\bar{t}$ production with rare decay mode $t\bar{t} \to tH\bar{q}$. The other labels denote the backgrounds.

D. Simulation results

In this subsection, we discuss the numerical results after imposing kinematic cuts. We need to include the QCD NLO corrections to the decay as well. As a result, we find that these corrections reduce the cross sections by about 50% for the g_{ut} coupling induced process and by about 100% for the g_{ct} coupling induced process, respectively. The corresponding results are listed in Table III. K_{pro} only includes the NLO corrections to the tH associated production, while K_{tot} also contains the NLO corrections to decay. The complete QCD NLO corrections are 11% for $ug \to tH$ and almost vanish for $cg \to tH$.

TABLE II. Kinematic cuts in the event selection.

Basic cut	$p_{T_j} > 25$ GeV, $p_{T_l} > 25$ GeV, $\not{E}_T > 25$ GeV, $\lvert\eta_{l,j}\rvert < 2.5$, $\Delta R_{bl,jl,bj} > 0.4$
H_T	$H_T > 200$ GeV
$m_{t,r}$	$\Delta m_t < 20$ GeV
$m_{H,r}$	$\Delta m_H < 20$ GeV
$y_{H,r}$	$\lvert y_{H,r}\rvert > 1.0$

We list the results after imposing various kinematic cuts in Table IV. For the $ug \to tH$ process, the clear signal with the coupling $g_{ut} = 0.2$ can be observed at the 5σ C.L. when the integrated luminosity is 100 fb^{-1} at the LHC. Here we define the discovery significance as $\mathcal{S}/\sqrt{\mathcal{B}} = 5$ and exclusion limits as $\mathcal{S}/\sqrt{\mathcal{S}+\mathcal{B}} = 3$, where $\mathcal{S}$ and $\mathcal{B}$ are the expected events numbers of the signal and the backgrounds. However, for the $ug \to tH$ process, the cross section of the process $t\bar{t} \to tH\bar{c}$ is about 2 times larger than that of the process $cg \to tH$ after cuts. As stated before, we choose data from the fifth column of Table IV. As a result, the 5σ C.L. discovery sensitivity of g_{ct} is 0.294 when the integrated luminosity is 100 fb^{-1} and $m_H = 125$ GeV.

We show the 5σ discovery sensitivities to FCNC couplings with several Higgs boson mass for different luminosities in Fig. 13. For a lighter Higgs boson, the cross sections become larger, but the branching ratio rates of $\text{Br}(H \to b\bar{b})$ get lower. When $m_H = 115$ GeV and integrated luminosity is 100 fb^{-1}, the limit on the g_{ut} coupling is 15% smaller than that for $m_H = 125$ GeV. In contrast, when the Higgs boson mass increases to $m_H = 130$ GeV, the limit is increased by 12.3%. The g_{ct} coupling has the similar behavior.

TABLE III. The LO cross sections and K factors of the tH associated production at the LHC ($g_{qt} = 0.2$) with the kinematic cuts in Table II applied. We define K_{pro} and K_{tot} to be the K factor of the process of tH associated production and the processes including production and decay, respectively. We apply all cuts for the g_{ut} coupling induced process. But for the g_{ct} coupling induced process, we do not apply the rapidity cut on the reconstructed Higgs boson.

	σ_{LO} [fb]	K_{pro}	K_{tot}
tug	6.64	1.22	1.11
tcg	0.428	1.40	1.00

TABLE IV. Cross sections (in fb) after imposing cuts for NLO tH, $tH(\bar{q})$ signal, and their backgrounds $t\bar{t}$, $Wb\bar{b}j$, $Wjjj$, and WZj. The cut acceptance $\epsilon_{\rm cut}$ is also listed. The b-tagging efficiency has been taken into account in the basic cut.

	Basic cut	H_T	$m_{t,r}$	$m_{H,r}$	$y_{H,r}$	$\epsilon_{\rm cut}$
$ug \to tH$ (NLO)	3.54	3.26	2.86	2.22	1.59	44.9%
$cg \to tH$ (NLO)	0.40	0.354	0.322	0.240	0.09	22.5%
$t\bar{t} \to tH\bar{q}$ (LO)	0.993	0.956	0.849	0.487	0.193	19.4%
$t\bar{t}$	21.0	19.9	17.3	9.55	3.89	18.5%
$W^+b\bar{b}j$	3.30	2.32	1.38	0.336	0.146	4.4%
W^+Zj	0.215	0.160	0.099	0.023	0.010	4.7%
W^+jjj	0.085	0.064	0.038	0.009	0.004	4.7%

If no signal is observed, it means that the FCNC Htq couplings can not be too large. In Fig. 14, we show the 3σ exclusion limits of couplings with several Higgs boson masses for different luminosities. The upper limits on the size of FCNC couplings are given as $g_{ut} \leq 0.121$ and $g_{ct} \leq 0.233$ with $m_H = 125$ GeV. These limits can be converted to the 3σ C.L. upper limits on the branching ratios of top quark rare decays [5,49] as follows:

$$\begin{aligned} \mathrm{Br}(t \to Hu) &\leq 4.1 \times 10^{-4}, \\ \mathrm{Br}(t \to Hc) &\leq 1.5 \times 10^{-3}. \end{aligned} \tag{54}$$

VI. CONCLUSION

In conclusion, we have investigated the signal of the tH associated production via the FCNC Htq couplings at the LHC with $\sqrt{S} = 14$ TeV, including complete QCD NLO corrections to the production and decay of top quark and Higgs boson. Our results show that the NLO corrections reduce the scale dependences of the total cross sections, and increase the production cross sections by 48.9% and 57.9% for the Htu and Htc couplings induced processes, respectively. After kinematic cuts are imposed on the decay products of the top quark and the

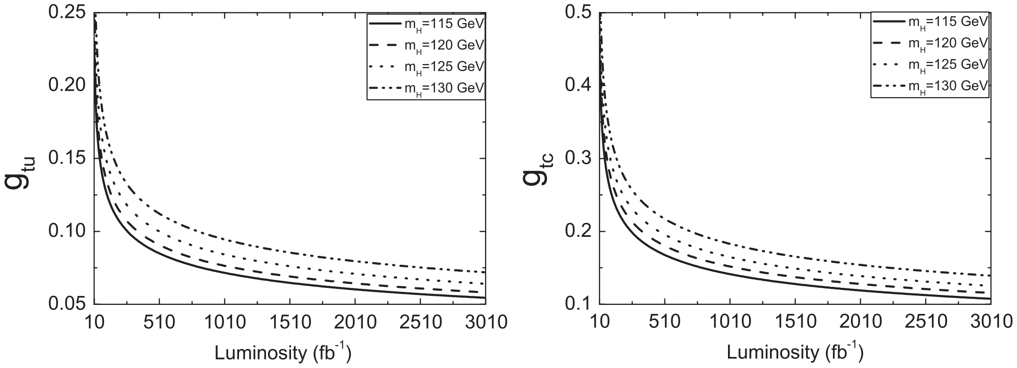

FIG. 13. The 5σ C.L. discovery sensitivities to the FCNC Htq couplings. The lines from bottom to top correspond to the m_H from 115 to 130 GeV.

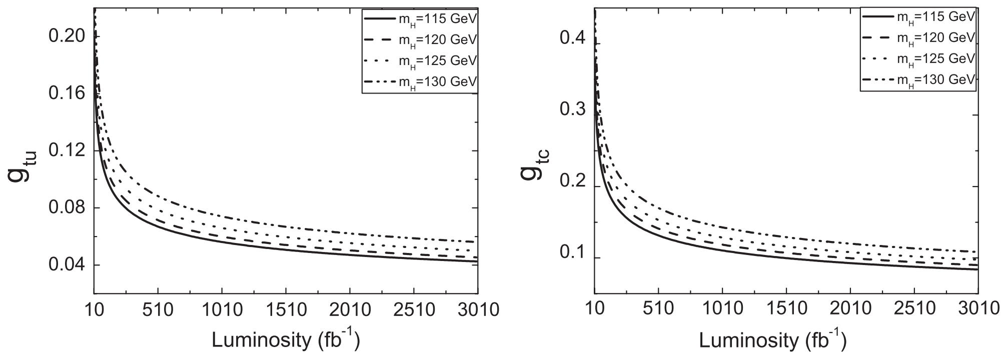

FIG. 14. The 3σ C.L. exclusion limits to the Htq couplings. The lines from bottom to top correspond to the m_H from 115 to 130 GeV.

TABLE V. Behavior of the sensitivity to the FCNC g_{ut} couplings as a function of Δm_H cuts at the 5σ level.

Δm_H	<5 GeV	<10 GeV	<15 GeV	<20 GeV	<25 GeV
Sensitivity to g_{ut}	0.180	0.159	0.157	0.150	0.335

Higgs boson, the NLO corrections are reduced to 11% for the Htu coupling induced process and almost vanish for the Htc coupling induced process. For the signal, we discuss the Monte Carlo simulation results for the signal and corresponding backgrounds, including the process of top quark pair production with one of the top quarks decaying to Hq as well, and show that the NP signals may be observed at the 5σ level in some parameter regions. Otherwise, the 3σ upper limits on the FCNC couplings can be set, which can be converted to the constraints on the top quark rare decay branching ratios.

ACKNOWLEDGMENTS

This work was supported by the National Natural Science Foundation of China, under Grants No. 11021092, No. 10975004, and No. 11135003.

APPENDIX

In this appendix, we numerically check the mass cut of the reconstructed particles. As stated before, the emission of an extra gluon broadens the mass distributions of reconstructed particles and makes b jet softer, which decreases the K factor of QCD NLO corrections when imposing reconstructing mass cuts or b jet p_t cuts. The more strict mass cuts are imposed, the smaller cross sections we get. On the contrary, if the mass cuts are loose, though the cross sections are larger, more background events are also to be considered, which may decrease the signal to background ratio. As a result, it is difficult to choose mass cuts on the reconstructed particles. We have checked that when we change Δm_H from <5 GeV to <25 GeV, the sensitivity to the g_{ut} coupling at the 5σ level is the lowest when $\Delta m_H < 20$ GeV, as shown in Table V. It confirms our choice in Eq. (51).

[1] S. Chatrchyan *et al.* (CMS Collaboration), Phys. Lett. B **716**, 30 (2012).

[2] G. Aad *et al.* (ATLAS Collaboration), Phys. Lett. B **716**, 1 (2012).

[3] S. Glashow, J. Iliopoulos, and L. Maiani, Phys. Rev. D **2**, 1285 (1970).

[4] G. Blankenburg, J. Ellis, and G. Isidori, Phys. Lett. B **712**, 386 (2012).

[5] J. Aguilar-Saavedra, Acta Phys. Pol. B **35**, 2695 (2004).

[6] F. del Aguila, J. Aguilar-Saavedra, and L. Ametller, Phys. Lett. B **462**, 310 (1999).

[7] J. Aguilar-Saavedra, Phys. Lett. B **502**, 115 (2001).

[8] J. Aguilar-Saavedra and G. Branco, Phys. Lett. B **495**, 347 (2000).

[9] J. J. Liu, C. S. Li, L. L. Yang, and L. G. Jin, Phys. Rev. D **72**, 074018 (2005).

[10] J. J. Zhang, C. S. Li, J. Gao, H. Zhang, Z. Li, C.-P. Yuan, and T.-C. Yuan, Phys. Rev. Lett. **102**, 072001 (2009).

[11] J. Gao, C. S. Li, J. J. Zhang, and H. X. Zhu, Phys. Rev. D **80**, 114017 (2009).

[12] Y. Zhang, B. H. Li, C. S. Li, J. Gao, and H. X. Zhu, Phys. Rev. D **83**, 094003 (2011).

[13] B. H. Li, Y. Zhang, C. S. Li, J. Gao, and H. X. Zhu, Phys. Rev. D **83**, 114049 (2011).

[14] J. M. Yang, Ann. Phys. (N.Y.) **316**, 529 (2005).

[15] S. Bejar, J. Guasch, and J. Sola, Nucl. Phys. **B675**, 270 (2003).

[16] J.-j. Cao, G.-l. Liu, and J. M. Yang, Eur. Phys. J. C **41**, 381 (2005).

[17] J. Guasch and J. Sola, Nucl. Phys. **B562**, 3 (1999).

[18] S. Bejar, J. Guasch, and J. Sola, Nucl. Phys. **B600**, 21 (2001).

[19] J.-M. Yang and C.-S. Li, Phys. Rev. D **49**, 3412 (1994).

[20] G. de Divitiis, R. Petronzio, and L. Silvestrini, Nucl. Phys. **B504**, 45 (1997).

[21] J. Diaz-Cruz, H.-J. He, and C. Yuan, Phys. Lett. B **530**, 179 (2002).

[22] J. Cao, G. Eilam, K.-i. Hikasa, and J. M. Yang, Phys. Rev. D **74**, 031701 (2006).

[23] R. Gaitan, O. Miranda, and L. Cabral-Rosetti, AIP Conf. Proc. **857**, 179 (2006).

[24] A. Arhrib and W.-S. Hou, J. High Energy Phys. 07 (2006) 009.

[25] A. Fernandez, C. Pagliarone, F. Ramirez-Zavaleta, and J. Toscano, J. Phys. G **37**, 085007 (2010).

[26] J. I. Aranda, A. Cordero-Cid, F. Ramirez-Zavaleta, J. J. Toscano, and E. S. Tututi, Phys. Rev. D **81**, 077701 (2010).

[27] F. Larios, R. Martinez, and M. A. Perez, Phys. Rev. D **72**, 057504 (2005).

[28] T. Plehn, Phys. Rev. D **67**, 014018 (2003).

[29] C. Weydert, S. Frixione, M. Herquet, M. Klasen, E. Laenen, T. Plehn, G. Stavenga, and C. D. White, Eur. Phys. J. C **67**, 617 (2010).

[30] S.-h. Zhu, Phys. Rev. D **67**, 075006 (2003).

[31] M. Klasen, K. Kovarik, P. Nason, and C. Weydert, arXiv:1203.1341.

[32] B. W. Harris and J. F. Owens, Phys. Rev. D **65**, 094032 (2002).

[33] J. J. Zhang, C. S. Li, J. Gao, H. X. Zhu, C.-P. Yuan, and T.-C. Yuan, Phys. Rev. D **82**, 073005 (2010).

[34] G. Passarino and M. Veltman, Nucl. Phys. **B160**, 151 (1979).

[35] A. Denner, Fortschr. Phys. **41**, 307 (1993).

[36] R. K. Ellis and G. Zanderighi, J. High Energy Phys. 02 (2008) 002.

[37] J. C. Collins, D. E. Soper, and G. F. Sterman, Nucl. Phys. **B261**, 104 (1985).

[38] G. T. Bodwin, Phys. Rev. D **31**, 2616 (1985).

[39] M. S. Carena, D. Garcia, U. Nierste, and C. E. Wagner, Nucl. Phys. **B577**, 88 (2000).

[40] P. Meade and M. Reece, arXiv:hep-ph/0703031.

[41] A. Denner, S. Heinemeyer, I. Puljak, D. Rebuzzi, and M. Spira, Eur. Phys. J. C **71**, 1753 (2011).

[42] Q.-H. Cao, R. Schwienhorst, and C.-P. Yuan, Phys. Rev. D **71**, 054023 (2005).

[43] J. M. Campbell, R. K. Ellis, and F. Tramontano, Phys. Rev. D **70**, 094012 (2004).

[44] J. Gao, C. S. Li, L. L. Yang, and H. Zhang, Phys. Rev. Lett. **107**, 092002 (2011).

[45] G. Aad *et al.* (ATLAS Collaboration), arXiv:0901.0512.

[46] M. Cacciari, G. P. Salam, and G. Soyez, J. High Energy Phys. 04 (2008) 063.

[47] J. Alwall, P. Demin, S. de Visscher, R. Frederix, M. Herquet, F. Maltoni, T. Plehn, D. L. Rainwater, and T. Stelzer, J. High Energy Phys. 09 (2007) 028.

[48] M. L. Mangano, M. Moretti, F. Piccinini, R. Pittau, and A. D. Polosa, J. High Energy Phys. 07 (2003) 001.

[49] C. S. Li, R. J. Oakes, and T. C. Yuan, Phys. Rev. D **43**, 3759 (1991).